ADVANCED FUNCTIONA MATERIALS
www.afm-journal.d

Exploiting Phonon-Resonant Near-Field Interaction for the Nanoscale Investigation of Extended Defects

Benedikt Hauer, Claire E. Marvinney, Martin Lewin, Nadeemullah A. Mahadik, Jennifer K. Hite, Nabil Bassim, Alexander J. Giles, Robert E. Stahlbush, Joshua D. Caldwell, and Thomas Taubner**

The evolution of wide bandgap semiconductor materials has led to dramatic improvements for electronic applications at high powers and temperatures. However, the propensity of extended defects provides significant challenges for implementing these materials in commercial electronic and optical applications. While a range of spectroscopic and microscopic tools have been developed for identifying and characterizing these defects, such techniques typically offer either technique exclusively, and/or may be destructive. Scattering-type scanning near-field optical microscopy (s-SNOM) is a nondestructive method capable of simultaneously collecting topographic and spectroscopic information with frequency-independent nanoscale spatial precision (≈20 nm). Here, how extended defects within 4H-SiC manifest in the infrared phonon response using s-SNOM is investigated and the response with UV-photoluminescence, secondary electron and electron channeling contrast imaging, and transmission electron microscopy is correlated. The s-SNOM technique identifies evidence of step-bunching, recombination-induced stacking faults, and threading screw dislocations, and demonstrates interaction of surface phonon polaritons with extended defects. The results demonstrate that phonon-enhanced infrared nanospectroscopy and spatial mapping via s-SNOM provide a complementary, nondestructive technique offering significant insights into extended defects within emerging semiconductor materials and devices and thus serves as an important diagnostic tool to help advance material growth efforts for electronic, photonic, phononic, and quantum optical applications.

1. Introduction

Wide-bandgap semiconductors are of current interest for high power, high temperature, and high frequency electronics due to their superior electrical and in some cases thermal characteristics in comparison to silicon.[1] While silicon carbide (SiC) is established as a material for commercial use in high power and high temperature electronics,[2] current emerging materials for these applications include gallium nitride (GaN) and gallium oxide (Ga_2O_3).[3] In the past, a consistent limiting factor for SiC-based high power, high temperature, and even optical devices was the propensity of the material for defect formation due to the similar formation energies of its many polytypes.[2a,4] Such defects led to significant degradation of the devices,[2a,5] requiring extensive materials and device studies to determine the correlation between the degradation and the specific defect(s). Emerging materials such as Ga_2O_3 and GaN also exhibit a large number of defects formed during growth,[3a,b,6] such as threading dislocations, stacking faults, and twin boundaries, which could lead to similar degradation of devices using these materials. For emerging materials, developing a quick and comprehensive method for understanding how such defects interact with free carriers, phonons, and incident light on the length-scale of the defect itself promises to improve the performance of high power, high temperature, optical, and quantum devices based on these materials. Furthermore, while SiC is now a rather mature material for power electronics applications, implementation as a material of choice for infrared

---

Dr. B. Hauer, M. Lewin, Prof. T. Taubner
Institute of Physics (IA)
RWTH Aachen University
52056 Aachen, Germany
E-mail: taubner@physik.rwth-aachen.de

The ORCID identification number(s) for the author(s) of this article can be found under https://doi.org/10.1002/adfm.201907357.

DOI: 10.1002/adfm.201907357

Dr. C. E. Marvinney, Prof. J. D. Caldwell
Department of Mechanical Engineering
Vanderbilt University
2400 Highland Ave, Nashville, TN 37212, USA
E-mail: josh.caldwell@vanderbilt.edu

Dr. C. E. Marvinney
Quantum Information Science Group
Oak Ridge National Laboratory
1 Bethel Valley Rd, Oak Ridge, TN 37830, USA

Dr. N. A. Mahadik, Dr. J. K. Hite, Dr. A. J. Giles, Dr. R. E. Stahlbush
US Naval Research Laboratory
4555 Overlook Ave, S.W., Washington, DC 20375, USA

Prof. N. Bassim
Department of Materials Science and Engineering
McMaster University
Hamilton, ON L8S 4L8, Canada

(IR) nanophotonic devices[7] or quantum information science applications[8] are still in their nascent phases and thus, would also benefit from gaining further insights into defect, free carrier and phonon interactions at the nanoscale. Here we correlate well-established spectroscopic and microscopic imaging methods for characterizing extended defects, including UV-photoluminescence (UV-PL), secondary electron (SE) imaging, electron channeling contrast imaging (ECCI), and transmission electron microscopy (TEM) with the emerging IR spectroscopic imaging method of scattering-type scanning near-field optical microscopy (s-SNOM) in order to provide complementary, sub-diffraction, spectroscopic and nanoscopic characterization of extended defects. To demonstrate the potential of this method, we focus on investigations using well-understood defects within 4H-SiC epitaxial layers as a means to benchmark the capabilities in this regard. Based on the preliminary work discussed here, it is clear that s-SNOM offers significant promise as a characterization technique for extended defects in Ga_2O_3, GaN, and other emerging materials.

To date, the investigations of SiC defects have focused on the spectroscopic and microscopic characteristics of the defects separately.[9] Multiple spectroscopic techniques, including electroluminescence (EL) and photoluminescence (PL) imaging,[9b,10] have been employed for these studies successfully, with the gold standard for defect identification and spatial mapping of the defect location being UV-PL. This method provides large-scale imaging of defects at visible emission frequencies, providing information regarding the spatial shape and location of the defect via its emission response.[11] Advanced UV-PL imaging enables the collection of spectral images with predefined spectral filters, providing coarse spectral information in concert with the spatial distribution via multispectral imaging of the defects present across an entire sample.[10a,12] More advanced methods, for instance using rotating double Bragg gratings, offer the potential for true hyperspectral imaging.[11] However, the spatial resolution of these methods are inherently limited by diffraction to at best a few hundred nanometers in the visible, but more typically on the order of a micron with standard microscope objectives. Therefore, these methods are not capable of providing truly nanoscale-resolved information at the defect length-scales. To obtain nanoscale resolution, electron beam techniques are often used, such as cathodoluminescence,[13] TEM[14] or scanning electron microscopy (SEM).[15] Electron beam methods also include the powerful, but lesser-known ECCI technique that has been explored for strain contrast imaging.[16] In this method, the sample is tilted to an angle with respect to the electron beam that is slightly deviated from the Bragg condition. This enables high contrast imaging of extended defects such as threading dislocations. ECCI had been established for defect analysis in metals and ceramics, but more recently has been demonstrated for studying defects in wide bandgap semiconductors through the pioneering work of Picard and coworkers for semiconductors such as GaN and SiC.[15a,17] This has allowed for nondestructive imaging of dislocations, grain boundaries, and topological information on a length-scale consistent with device dimensions.[18] However, while ECCI offers significant enhancements in contrast for imaging of extended defects with nanoscale precision, it offers no spectroscopic information, which is necessary for identifying the origin and influence of the defect upon electronic and optical properties of the material. Thus, a method that provides both nanoscale spatial resolution *and* spectroscopic information on the same length scale would enable more efficient and precise defect analysis than is currently available.

One such method is s-SNOM. In s-SNOM, a monochromatic laser is focused onto a metalized atomic force microscope (AFM) tip operating in tapping-mode. Due to the nanoscale size of the tip apex, evanescent near-fields are excited at the tip and the near-field interaction of tip and sample is confined to a region of about 20 nm (tip radius of curvature).[19] Here the tip acts as a local antenna and in order to obtain 2D maps of the near-field interaction the tip is scanned relative to the sample surface, while detecting the back-scattered light. The back-scattered light depends on the near-field interaction of tip and sample, which is influenced by the local dielectric function of the sample. The complex nature of the dielectric function leads to a complex scattering signal, causing significant contributions to both the amplitude as well as the phase signal of the scattering signal. Using a pseudo-heterodyne interferometric setup and higher-harmonic demodulation, the pure near-field amplitude and phase of the scattered light can be extracted at each pixel.[20] Similar to reflection and absorption spectra in Fourier-transform infrared spectroscopy,[21] both near-field amplitude and phase provide complimentary information. The near-field interaction of tip and sample can be modeled by a dipolar coupling of charges in the tip with image charges in the sample. It shows a resonance in the amplitude and phase signal of the scattered light for frequencies close to a certain, negative permittivity $\mathrm{Re}[\varepsilon(\omega)] \approx -1 \ldots -3$, which is the case for fundamental excitations in solids such as typically observed for charge carrier oscillations and phonons in the infrared spectral range.[19a,22] Light can also couple to these excitations forming hybrid propagating interface modes called polaritons (e.g., surface phonon polaritons and surface plasmon polaritons),[7a,23] which can be detected using s-SNOM as the scattered field also depends on the local electric field strength.[22b,24]

To extract the spectral response, the sample can be probed at multiple discrete incident frequencies of the focused laser in succession to plot the frequency-dependent s-SNOM amplitude and/or phase, providing a map of the spatial variation in the s-SNOM response at each frequency.[22b] Thus, s-SNOM provides obvious benefits for high resolution defect imaging when monitored at mid-IR frequencies as it provides the potential to i) investigate the impact of defects upon the free-carrier density[25] or polaritonic behaviors,[26] ii) provide information regarding crystalline structure and polytype,[27] and iii) determine the role such defects play in the performance of nanophotonic devices such as polaritonic antennas,[28] waveguides,[29] and metasurfaces.[30] While s-SNOM should not be expected to replace the previously mentioned spectroscopic and microscopic methods, it instead provides a noninvasive technique offering complementary IR spectroscopic information about the defect(s) and surrounding regions of interest, while simultaneously imaging the topography of the sample.

For this study, we have chosen 4H-SiC to demonstrate the potential for s-SNOM as a tool for extended defect investigations, enabling noninvasive and simultaneous collection of spectroscopic and spatial information. Our reasons are threefold: First, i) SiC is an established wide bandgap semiconductor material that can host a broad variety of extended defects,[9] providing the opportunity to demonstrate the capabilities of s-SNOM to probe such defects with nanoscale precision in comparison to conventional methods for well characterized defects and materials. Further, while SiC is established for electronic applications, it is currently also of emerging interest for ii) quantum information science applications[8,31] and for iii) surface phonon polariton (SPhP) based optical devices.[7a,32] The interest in (ii) results from measurements of bright, room-temperature single-photon emitters within SiC,[31] which could be useful for quantum computation,[33] quantum key distribution,[34] and quantum sensing.[31a] The interest in (iii) results from SiC being a polar semiconductor with a broad Reststrahlen band (≈790–970 cm^{-1}; 12.6–10.3 µm for 4H-SiC), where SPhPs are supported.[7a] This enables potential novel devices such as compact modulated IR sources and switches,[30,35] and highly focused modes for nanophotonic circuits and on-chip IR components.[7a] The s-SNOM technique has already demonstrated that near-field studies of SiC can distinguish between different polytypes,[27a] strain,[27b] and crystalline quality[36] within the Reststrahlen band, suggesting that these near-field techniques will also allow for insightful characterization of extended defects. Additionally, while the s-SNOM technique has recently been employed to study fundamental material properties of semiconductors and/or phase change materials other than SiC,[37] such as GaN,[38] hexagonal boron nitride (hBN),[24c,d,28,39] vanadium dioxide (VO$_2$),[30] Ge$_3$Sb$_2$Te$_6$ (GST),[32c] and Ag$_4$In$_3$Sb$_{67}$Te$_{26}$ (AIST),[40] a detailed, correlative study of extended defects in wide-bandgap materials has not been performed up until now.

2. Results and Discussion

For the studies discussed here, a 1 cm^2 chip of a 50 µm thick 4H-SiC unintentionally doped ($N_d \approx 1 \times 10^{14}$ cm^{-3}) epitaxial layer grown on a highly doped 4H-SiC substrate ($N_d \approx 3 \times 10^{18}$ cm^{-3}) with an 8° off-normal (*c*-axis) surface plane in the [11–20] direction was used.[4a] To identify the locations of various defects, a UV-PL map, constructed of multiple ≈1.2 mm^2 PL images over the entire square sample was collected (**Figure 1**a). The UV-PL was collected through a 590 nm long-pass filter, which highlights the spectral emission associated with a variety of dislocations and extended defects in 4H-SiC, such as the partial dislocations that bound recombination-induced stacking faults (RISFs),[13] low-angle grain boundaries, threading dislocations which are either threading screw (TSDs) or threading edge dislocations (TEDs),[12a] Basal plane dislocations,[11c] carrot defects,[12b] and micropipe defects.[11c] We highlight two regions of interest with the dashed yellow and blue boxes, and provide a higher resolution image encompassing these areas (Figure 1b), detailing where the defects studied in this work are located. The first (Region 1) corresponds to the location of a carrot defect, while the second (Region 2) designates the position of a cluster of micropipe defects confined within a larger arrow defect.[14b] Through comparison of microscopic and spectroscopic characterization of the various defects in these regions of interest with the s-SNOM response, we aim to benchmark the power of this technique for such studies. Within this context, the other characterization tools employed include UV-PL, SEM with SE, ECCI, and TEM. We propose this as the next step in developing s-SNOM as an emerging tool in semiconductor material and potentially device characterization.

2.1. Defect Selection

In epitaxial SiC growth, there are a broad variety of extended defects that have warranted study over the years. However, for the first s-SNOM demonstration of extended defect characterization, it is important to find defects that exhibit a surface morphological feature for easy correlation between the well-known characterization tools of TEM and UV-PL with s-SNOM, but

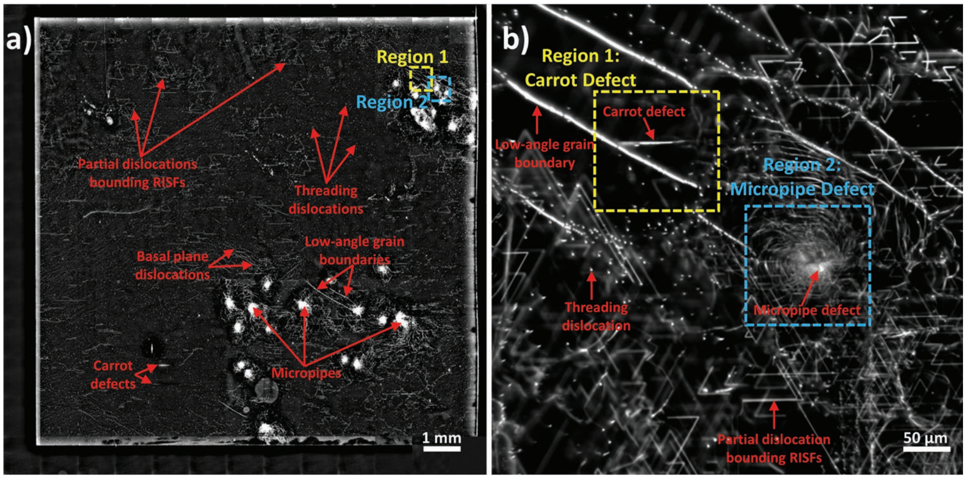

Figure 1. Conventional UV-photoluminescence. a) The full UV-PL map of the full 4H-SiC sample and b) a higher resolution UV-PL image of the region of interest, both with a 590 nm band-pass filter. The two general regions in which s-SNOM mapping was acquired are marked with yellow (carrot defect) and blue (micropipe defect associated with an arrow defect) squares. Red arrows in both figures indicate identified defects, including partial dislocations bounding recombination induced stacking faults (RISFs), threading dislocations, Basal plane dislocations, low-angle grain boundaries, additional carrot defects, and additional micropipe defects.

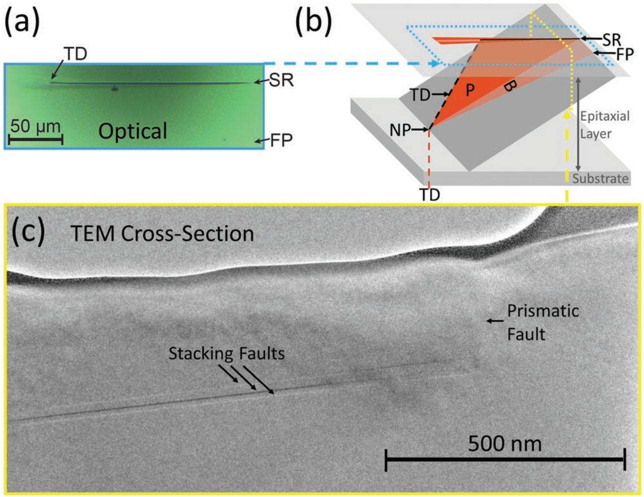

Figure 2. Carrot defect. a) A conventional optical microscope image of the carrot defect studied in this paper, with the estimated positions of different line defects marked with arrows. b) A schematic of a carrot defect, with the associated defects marked. The carrot nucleates from a threading dislocation (TD) in the substrate, marked as the nucleation point (NP). Two stacking faults called prismatic fault (P) and basal plane dislocation (B) intersect in a stair-rod dislocation (SR). At the opposite edge, the P [B] is bounded by a TD [Frank partial dislocation (FP)]. c) A transmission electron microscopy cross section of the carrot defect, taken near the SR defect, with the offcut direction (11–20) perpendicular to the sample/image plane. The diffraction contrast image shows two to three stacking faults in the middle of the carrot defect, corresponding to the B stacking fault and also additional recombination-induced stacking faults. Finally, the P fault may be visible, due to imperfect TEM sample preparation.

that also have additional defects that agglomerate nearby for further study. Two well-known extended defects that meet this criteria are the carrot[14b,41] and the micropipe defects[42] that were identified in Regions 1 and 2 of the UV-PL map presented in Figure 1.

2.2. Carrot Defect

We first investigate the carrot defect located in Region 1 (Figure 1), as its spatial position is easily identifiable with optical microscopy due to the clear topographical features for which it is named (**Figure 2**a). The structural properties of the carrot defect have been previously investigated by Benamara et al.[14b] using KOH etching and cross-sectional TEM, and a representation of the known carrot structure is provided in Figure 2b. The carrot defect has been reported to nucleate at a threading dislocation [TD] present within the substrate that splits into multiple partial dislocations during epitaxial growth. As the threading dislocation propagates through the epilayer, a prismatic fault [P] forms perpendicular to the substrate in the (1–100)-plane, bounded by the threading dislocation and a stair-rod dislocation [SR]. A third partial dislocation, known as a Frank partial [FP], may also form at the nucleation point, establishing a basal plane fault [B] within the region between the Frank partial and stair-rod. This takes the form of an in-grown stacking fault lying in the 8° off-axis (0001)-plane, hence its inclined structure, whereby it is observed to grow at this angle from the nucleation point within the epilayer up to the epilayer surface.[12b] In-grown stacking faults can exhibit a range of stacking orders, each with different electronic structure, resulting in luminescence properties that differ from the surrounding epitaxial film.[13,43] A high-resolution TEM cross-section (the offcut (11–20) direction is perpendicular to the sample and image plane) of the stair-rod region of the extended carrot defect collected following the other nondestructive characterization methods is shown in Figure 2c. This TEM diffraction contrast image illustrates the presence of a bounded region of several stacking faults, the first of which is most likely the basal plane stacking fault. The second and/or third could be additional basal plane stacking faults, or could be RISFs running underneath the region of the extended carrot defect as such defects are evident from the UV-PL images of this spatial region and will be discussed further below. All of these stacking faults lie within a plane rotated 8° from the sample surface, as expected from the known 8° offcut of the 4H-SiC epitaxial layer surface. Additionally, all three of the stacking faults terminate on the right side of the TEM image, where we observe the intersection of the prismatic fault of the carrot defect with the TEM lamella.

2.3. Extended Defect Investigations via s-SNOM

The three main characteristic dislocations (threading dislocation, stair-rod, and Frank-partial) that we observe within the subject carrot defect have been investigated by s-SNOM and simultaneous AFM topography and were compared to ECCI and SE-SEM images (**Figure 3**). The orientation of the defects is as in Figure 2a. The s-SNOM maps were collected close to the maximum of the resonant phonon near-field interaction of 4H-SiC, which occurs at ≈934 cm^{-1}.[22b,27a] From the AFM topography, each of the threading [TD], stair-rod [SR], and Frank partial [FP] dislocations appears as a pit of depth 219, 89, and 45 nm, respectively, with visible morphological features in the form of bumps or ridges near each dislocation surface termination. For the s-SNOM and microscopy techniques, the threading, stair-rod, and Frank partial dislocations are clearly observable, as are some of the additional defects highlighted in Benamara et al.[14b] Specifically, both the threading dislocation and the connected prismatic fault [P] are observed in all five images (Figure 3a). All five images in Figure 3b illustrate that the prismatic fault connects to the stair-rod at the surface of the sample, and each images shows that the basal plane [B] extends down from the stair-rod. The other end of the basal plane is shown connecting to the Frank partial (Figure 3c), and in all five images a second clear line is observed extending to the left of the Frank-partial, which is assigned to another prismatic fault (marked P_2) connecting the Frank partial to a potential TSD.[44] In the following, the additional features and defects observed in these 15 images will be discussed.

We start by investigating the features of the threading (TD), stair-rod (SR), and Frank partial (FP) dislocations that appear in both the s-SNOM and the electron microscopy images in Figure 3 (here-in referred to by their acronyms for brevity). The first salient feature is the periodic arrow-shaped lines extending to the left of the dark TD region that exist in the s-SNOM

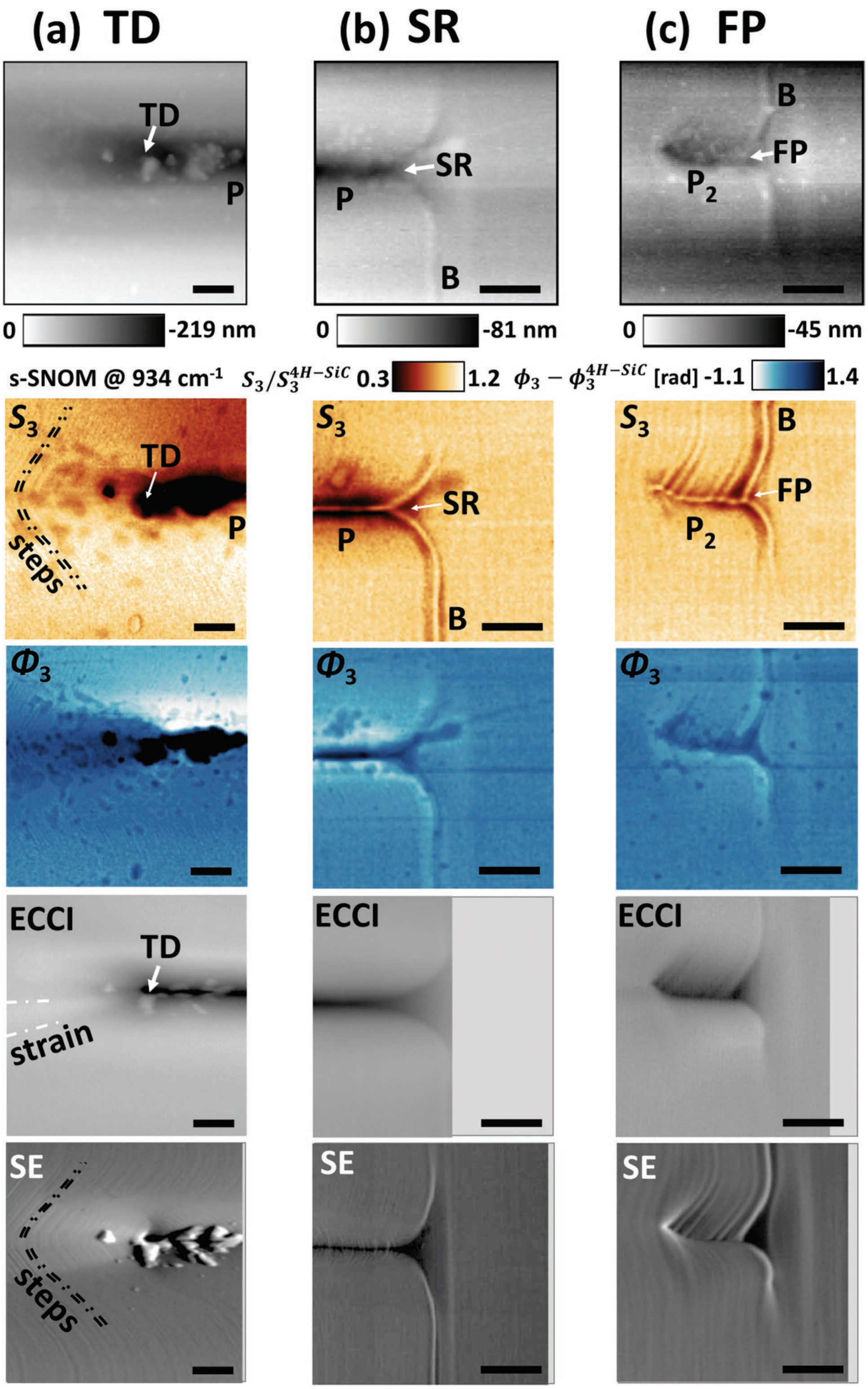

Figure 3. Carrot defect in s-SNOM versus conventional electron microscopy. The topography and near-field optical images recorded at 934 cm^{-1} for three characteristic carrot defect points: a) threading dislocation (TD), b) stair-rod dislocation (SR), and c) Frank-partial dislocation (FP). The near-field amplitude (S_3) and phase (Φ_3) color scales refer to all three image sets. ECCI and SE images are shown for comparison at all three locations, where the monotone light gray regions indicate regions that were not scanned with that technique. Important features such as step bunching (steps), strain, prismatic faults (P and P_2), and the basal plane (B) are marked. The scale bar is 500 nm for all 15 images.

amplitude image (but not the topography) and also show up more faintly in the SE image (Figure 3a). In both cases, the spacing of these step-like features is ≈58 nm. Similar step-like features of ≈67 nm are also observed in the s-SNOM and SE to the left of the FP dislocation, parallel to the basal plane dislocation where it intersects the sample surface (Figure 3c). Both of these step-like features surrounding the TD and FP are most likely due to step bunching, which consists of the coalescence of several smaller atomic steps into one larger, more energetically favorable step during epitaxial growth on off-axis substrates.[45] Prior works have demonstrated that step bunching for epitaxial 4H-SiC grown from an 8° off-normal (*c*-axis) substrate can have lateral widths of ≈20–70 nm,[45a] which agrees well with our experimentally observed feature widths. It should be noted that in principle, atomic steps such as step bunching may also be observed via ECCI,[18a,46] and are somewhat visible in Figure 3c above the secondary prismatic fault, where the sample surface is at the correct angle. However, imaging a larger area of these steps with ECCI requires the sample to be rotated so that the nonplanar surface in the vicinity of this defect can be held at the correct angle with respect to the detector[16] for imaging, which was not utilized in these measurements and is not readily available in most commercial SEMs. As such, s-SNOM provides an alternative, reliable method for characterizing step bunching, providing accurate measurements of the features.

Next we analyze the additional variations in contrast occurring over both the nanometer- and micron-scale that are observed in all three microscopy-based characterization techniques (s-SNOM, ECCI, and SE). Some variations in s-SNOM contrast can be assigned to topographic features, such as the surface scratch observed extending diagonally to the upper right of the SR dislocation (Figure 3b). However, others cannot, such as a large variation in near-field amplitude (phase) near the TD, where the amplitude (phase) changes from low (negative) in the region above TD, to high (positive) below (Figure 3a). The region of largest near-field phase contrast extends to the left of the TD, and exhibits a corresponding change in contrast in both the ECCI and SE images, but with no observable corresponding topographic feature identified in the AFM topography image. Previous s-SNOM investigations have shown that variations in strain,[27b] charge-carrier concentration,[25a] and polytype[27a] can induce such effects in the near-field contrasts. In ECCI however, such a bright-line charge contrast as is highlighted in Figure 3a is known to be due to subsurface strain,[16] most likely caused by the nucleation point of the TD[47] inducing the carrot defect. Thus, this contrast in s-SNOM, ECCI, and SE images to the left of the TD is assigned to strain variations, and illustrates that s-SNOM can also accurately detect such effects with similar spatial precision as the predominant microscopy methods.

So far, the robustness of the s-SNOM technique is illustrated with its comparison to the SE and ECCI techniques, as the salient features within the carrot defect that are observed are all also identified using s-SNOM. However, there are two additional features surrounding the three characteristic dislocations that are observed only in the s-SNOM amplitude and phase plots, implying that further information beyond those present in the conventional electron microscopy techniques can also be simultaneously extracted. First, while in the ECCI and SE techniques both of the prismatic faults, the SR, and the FP appear dark, in s-SNOM these four defects have a dark-bright-dark (bright-dark-bright) variation in amplitude (phase) (Figure 3b,c). These variations in contrast within the s-SNOM maps could originate from a change in structural order due to the presence of RISFs having propagated into the vicinity of the prismatic fault,[27a] and initial evidence for this claim is present in the TEM of the extended carrot defect, where potential RISFs are observed (Figure 2c). Second, all three sets of s-SNOM phase images have dark spots scattered around the TD, SR, and FP defects that do not appear in any of the ECCI or SE images, although most of these spots are noticeable in the AFM topography (Figure 3a–c), see Section S3 (Supporting Information) for detailed comparisons. The large contrast of these features in the near-field phase images (and also in the TD near-field amplitude) could indicate localized strain, potentially indicating that these features are the result of TSDs and TEDs that terminate at the sample surface.[44,48] It should be noted that clear observation and identification of TSD/TEDs using nondestructive techniques has been problematic, with investigations using multispectral luminescence imaging providing the best delineation,[12a] while unambiguous identification has only been possible using molten KOH etching of the defects.[41] No technique is ideal, as AFM can only identify TSDs and not TEDs,[49] the spatial resolution of optical measurement approaches are diffraction limited, and KOH etching is destructive. Here, the presence of these defects, potentially TSDs though not TEDs as they have no topographical features, might be able to be identified in a single s-SNOM map, depending on the incident frequency as we discuss below.

2.4. Spectral Dependence of s-SNOM Response from Extended Defects

One of the primary advantages of the s-SNOM technique is the ability to tune the frequency of the incident light with respect to fundamental material excitations, such as the Reststrahlen band or the bandgap of the material. Thus, the frequency dependence of the near-field measurements should provide new nanoscale-resolved spectroscopic information about the defects within wide bandgap semiconductors such as SiC, adding an additional "knob" for such characterization. Thus, the region around the SR dislocation is compared using two frequencies of s-SNOM laser excitation in **Figure 4**a,b, providing the amplitude (top) and phase (bottom) maps collected at a) 891 cm^{-1} and b) 944 cm^{-1}. At 891 cm^{-1}, the dark spots in the amplitude and phase maps that were previously mentioned as possibly correlating with TSDs are clearly observed, however, at 944 cm^{-1} these features are almost completely absent in both plots, more noticeably in the amplitude. Such a varying spectral signature provides further evidence that these spots could have a strain related component[27b] are not simply the result of small morphological features and thus, supportive of our assignment as TSD to some of these features.

A common technique for obtaining spectral information about defects in wide bandgap semiconductors over large length scales is UV-PL. While s-SNOM near-field mapping creates a much higher resolution image of the region and thus allows the exact placement of spectral features to be

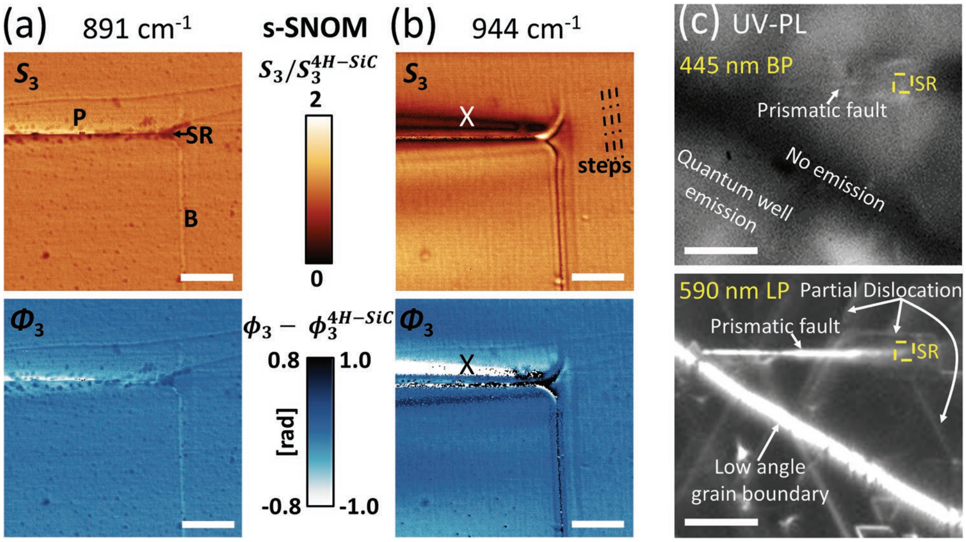

Figure 4. Near-field versus UV-PL. s-SNOM near-field images are shown for frequencies a) $\omega = 891$ cm^{-1} and b) $\omega = 944$ cm^{-1} in amplitude (top) and phase (bottom). The s-SNOM length scale bar is 1 µm and notice the slightly different scale for the s-SNOM phase images. The locations of the stair rod dislocation (SR), the prismatic fault (P), the basal plane dislocation (B), and step bunching (steps) are marked, as well as an additional feature marked X. In (c), UV-photoluminescence images are shown, with yellow dashed boxes indicating the region of the s-SNOM images. The UV-PL is shown in two frequency regimes using a 445 nm band-pass (BP) filter (top) and a 590 nm long-pass (LP) filter (bottom). The prismatic fault of the carrot defect, partial dislocations around the carrot, a low angle grain boundary, and quantum well emission contrast are marked. The UV-PL scale bar is 20 µm.

determined, UV-PL offers a much larger imaging field of view and provides spectral information about the defects that are present.[11c] Two UV-PL maps collected with different imaging filters for the region centered around the carrot defect (top: 445 nm band-pass filter, bottom: 590 nm long-pass filter) are provided in Figure 4c, where the yellow square represents the s-SNOM mapped region. In the UV-PL maps, extended defects that surround the carrot defect can be clearly observed as bright features, however, the small TSDs or even TEDs are not readily observed because the spectral features of these defects are weak in comparison to the other defects present. The most noticeable defects are the low-angle grain boundaries that have a very strong long wavelength emission (590 nm long pass), but are not observed at higher energies (445 nm band pass). The carrot defect itself is visible at both wavelengths (fainter in the 445 nm BP image) as a bright emission line resulting from the prismatic fault. Some defects associated with the carrot region bounded by the FP and SR dislocations also exhibit noticeable emission signatures in the UV-PL images collected with a 445 nm band-pass filter. The most common emission observed with the 445 nm band-pass filter, however, occurs as large, faint emission regions, bounded by regions of no emission (see Figure S1, Supporting Information, for further identification). These correlate to the spatial regions bound between the bright, lower-energy emission lines observable within the 590 nm long-pass image, which include the low-angle grain boundaries as well as a second type of smaller lines. These latter linear emission features correspond to the partial dislocations that bound RISFs.[12b,13] Inside a RISF, the SiC emits at a higher energy due to the formation of quantum wells due to the local 3C-SiC stacking order of the RISFs, which emit at an energy ≈0.25 eV below the conduction band edge of 4H-SiC.[50] This quantum well emission is what is most commonly observed in the 445 nm band-pass filter image in Figure 4c (additional identification in Figure S1, Supporting Information). The presence of these RISF features in the UV-PL corroborates the RISF features that we observed in both the TEM (Figure 2c) and the initial s-SNOM of the SR (the dark-bright-dark pattern in Figure 3b), and also appear to be present in the s-SNOM amplitude and phase image in Figure 4b, marked with an X.

Stacking fault defects consist of a local change in stacking order that can also be observed in s-SNOM because the phonon near-field response depends on polytype,[27a] and because such a change in stacking order is typically also correlated with local changes in strain and potentially carrier density.[4b] In the region marked X, located above the prismatic fault of the carrot defect in Figure 4b, there also exists a region of dark (bright) line contrast in the near-field amplitude (phase) maps that are only observed at 944 cm^{-1}. The contrast of this feature is not clearly observed by the other characterization techniques, including those presented in Figure 3b. However, through a comparison to the wider-field-of-view UV-PL image around this region (Figure 4c), it is apparent that the SR dislocation, including region X, is correlated to the spatial region located between the prismatic fault and a set of partial dislocations, indicating region X could be associated with RISFs present within the 4H-SiC that terminated at the epilayer surface near the carrot defect. The 3C-SiC (cubic) stacking order of such stacking faults in 4H-SiC could be the origin of the large contrast observed in the near-field images (Figure 4b) and would be consistent with the strong spectral dependence, as discussed by Huber et al.[27a] for polytype variations in SiC and is supported further by the observation of multiple stacking faults in the TEM cross-sectional image (Figure 2c). In the work by Huber et al., the authors demonstrated that different polytypes of SiC cause large variations in contrast in s-SNOM due to the shift in frequency of ω_{LO}. Thus, it is probable that the origin of the feature at X is indeed due to the presence of an RISF, likely nucleated from the substrate-epilayer surface, then extending up to the surface via propagating induced by the UV-illumination occurring during the UV-PL mapping of this region. This observation again indicates the power of s-SNOM as the low energy incident light provides the ability to observe, but not influence such defects, as can occur during UV excitation in UV-PL imaging.[51]

To evaluate the spectral signature of 3C stacking faults, we used the Finite Dipole Model[52] in combination with dielectric function data for 3C- and 4H-SiC.[53] The expected near-field amplitude spectra s_3/s_3^{Au} of both polytypes with respect to that of a highly reflective surface (here gold) are depicted in **Figure 5**a, while the corresponding near-field phase spectra $\phi_3–\phi_3^{Au}$ are provided in Figure 5b. Below 900 cm^{-1}, both polytypes show only a weak near-field signal and no considerable variation in contrast between the polytypes is expected (left inset). However, between 920–1000 cm^{-1} near the SPhP

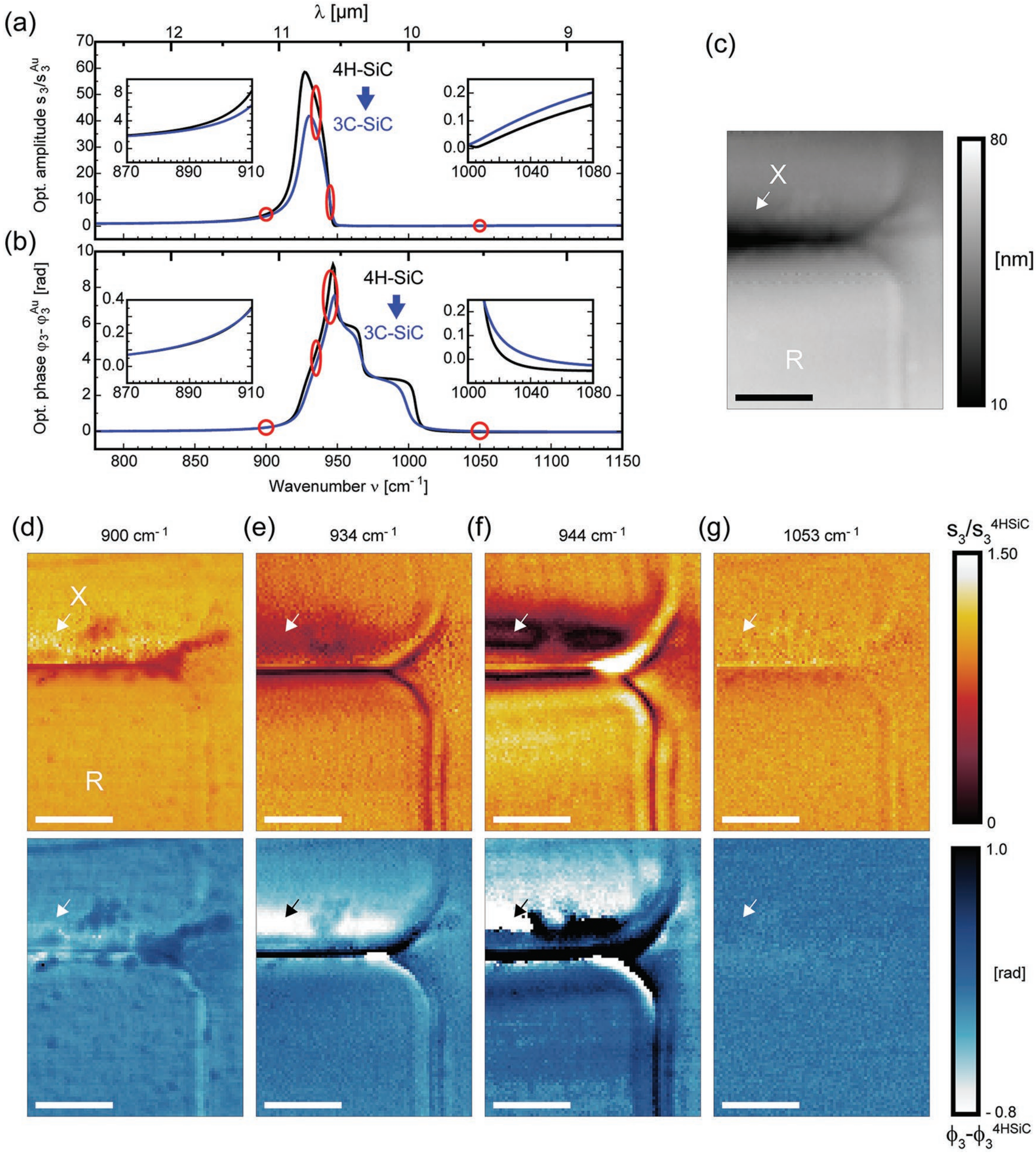

Figure 5. Spectral dependence of near-field contrast of 3C- and 4H-SiC near the stair rod dislocation. The normalized near-field a) amplitude and b) phase spectra of 3C- and 4H-SiC were calculated individually using the Finite Dipole Model[71] in combination with dielectric data of 3C- and 4H-SiC, which were experimentally obtained from far-field reflectivity studies. In both spectra, two insets with enhanced resolution depict the contrast below and above the phonon resonance. The red ellipsoids mark the wavenumber ν used in d) 900 cm^{-1}, e) 934 cm^{-1}, f) 944 cm^{-1}, and g) 1053 cm^{-1}. c) Topography image of the stair rod dislocation. The feature marked "X" is first identified in the discussion of Figure 4b, stems from a potential 3C stacking fault. d–g) Corresponding near-field optical amplitude (top) and phase (bottom) images. All images are both normalized to the surrounding response of defect-free 4H-SiC near "R." The scale bar in all images is 500 nm.

resonant conditions of these two polytypes, both 3C- and 4H-SiC exhibit a strong near-field phonon resonant response that differs in both amplitude and phase. Within 3C-SiC the near-field phonon resonance is both spectrally shifted and damped, making the phonon resonance considerably weaker in amplitude and phase than that of 4H-SiC. Thus, a reasonable contrast can be expected at the energies where s-SNOM was performed here. Outside the resonance spectral region, for instance at frequencies > 1000 cm^{-1}, the near-field amplitude and phase signals are again significantly reduced in comparison to the peak (right inset). Here, both amplitude and phase for 3C-SiC are slightly higher relative to 4H-SiC due to the shift of the phonon properties and differences in high frequency (ε_∞) contribution to the dielectric function. Thus, at high frequencies the contrast between the two polytypes should be inverted with respect to lower frequency maps.

To qualitatively verify whether the near-field feature X identified in Figure 4b can be attributed to a change in SiC polytype from 4H to 3C due to the presence of RISFs, the local infrared spectral response is probed using s-SNOM and compared to the calculated response. A topographic image of the region around the SR dislocation is provided in Figure 5c with a white arrow indicating the general location of the feature X, while the characteristic near-field contrast for 3C- and 4H-SiC is shown in Figure 5a,b. The same SR region is then sequentially imaged at the four frequencies marked by the red ellipsoids in Figure 5a,b: i) Below the SPhP resonance at 900 cm^{-1}; ii,iii) near the SPhP resonance at 934 and 944 cm^{-1}; iv) above the SPhP resonance at 1050 cm^{-1}. The SPhP resonance frequency falls within the Reststrahlen band (see Figure S2b, Supporting Information), and can be calculated as in Huber et al.[54] The corresponding near-field amplitude and phase images (to those in Figure 5a,b) are depicted in Figure 5c–f. While a rich variety of features can be observed at all frequencies, the spectral characteristics of feature X are some of the most prominent. Near the SPhP resonance at ω = 934 and 944 cm^{-1}, the feature X (above the SR) shows a significant dark (bright) amplitude (phase) contrast, which is associated with a significantly lower amplitude and phase signal than the surrounding 4H-SiC lattice (Figure 5e,f). When compared to an undisturbed region of 4H-SiC below the defect (region R), the amplitude signal is reduced by a factor of 2 and the phase undergoes a change of $\Delta\phi \approx \pi$. This large amplitude and phase contrast matches well with the calculated spectral response anticipated for a polytype change over a short spatial period with 3C- and 4H-SiC, where a smaller maximum near-field amplitude and phase is expected within a 3C-SiC RISF defect within 4H-SiC (Figure 5a,b). In accordance with the calculations, no significant near-field contrast can be observed either below (900 cm^{-1}) or above (1050 cm^{-1}) the SPhP resonance. While the contrast inversion expected at high frequencies is not observed (right inset Figure 5a,b), the weak signal strength in both of these spectral regions precluded quantitative confirmation of this comparison. Thus, in accordance with the calculated spectral response of 3C- and 4H-SiC, the experimental frequency-dependent near-field spectra, as well as the results by UV-PL (Figure 4c) and TEM cross-sectional imaging (Figure 3c), the extended defect above the SR can be attributed as resulting from RISFs.

We note that the increase in contrast of both polytypes at 944 cm^{-1} relative to that observed at 934 cm^{-1} does not fit to the calculated contrast of 3C- and 4H-SiC. However, in addition to a change of the polytype, the RISF can further distort the conduction band edge and create an inclined quantum well.[4b] This leads to a redistribution of charge carriers in the sample, causing them to accumulate in the quantum well defined by the RISF. As previously reported for grain boundaries in SrTiO_3, an accumulation of charge carriers at extended defects can lead to a similar damping of the phonon near-field resonance.[55] Furthermore, local stress and strain can significantly influence the phonon spectra as well.[27b,38] Strain is likely to play a significant role around lattice defects, and locations with increased strain have been observed around the extended carrot defect. Strain could be caused by a variation in the quality of the crystal and thus could also lead to increased phonon damping and a decrease in the near-field scattering amplitude, caused by a higher density of point defects in the sample, such as TSDs.[36] In order to fully separate all the different influences and unequivocally verify the spectral signatures that stem purely from the RISFs, a quantitative near-field analysis of normalized spectra is necessary. In general, the absolute s-SNOM scattering signal depends on the overall tip shape including shaft (acting as an antenna), which is difficult to model. However, the relative scattering signal with respect to a reference material depends on the tip radius and demodulation parameters only, and thus can be reliably evaluated. Similar to far-field Fourier-transform infrared reflectivity (FTIR) studies, s-SNOM spectra need to be normalized to reference spectra of a sample with a known constant infrared response (usually Si, Au) for quantitative analyses. In our case no such reference region was available close to the defects investigated. To derive quantitative values for the local stress/strain,[38] charge carrier accumulations,[55] or crystal quality[36] around the defects in future studies, nonresonant reference materials such as lithographically deposited Au patches with additional direct comparison to TEM or KOH etch-pit analysis are necessary.

2.5. Micropipe Defects

To demonstrate a broader range of defects that s-SNOM can detect and potentially identify, we next examine a cluster of micropipes associated with an arrow defect. Micropipes are a common defect defined by their hollow core[9a] and arrow defects also exhibit a large arrow-like morphological feature, which similar to the carrot defect, enables easy identification for the comparative studies discussed here. Additionally, like the carrot defect, the spatial region in the vicinity of both the micropipes and arrow defects commonly have many other extended defects, making a wide range of defect characterizations possible. Such a cluster of micropipe defects agglomerated in the vicinity of an arrow defect is provided using various spectroscopic imaging methods in **Figure 6**. The arrow defect is visible in the optical image (inset Figure 6a) as a forked line pointing left toward a group of associated micropipe defects within the primary UV-PL image. The micropipe defects are designated by multiple bright emission spots in the UV-PL and have been boxed in yellow. Topography and near-field mapping

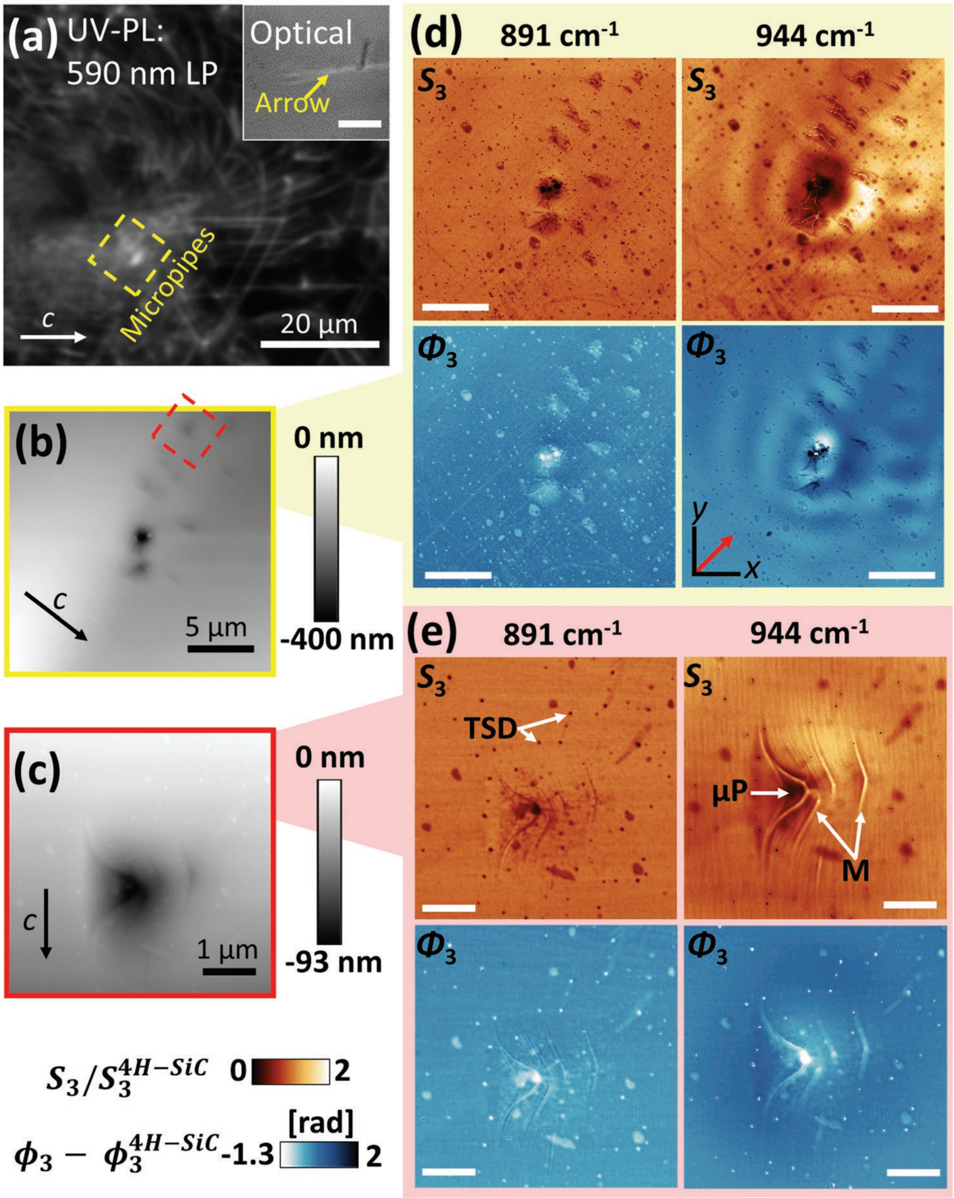

Figure 6. Additional defect characterization with s-SNOM and UV-PL. a) UV-PL (590 nm LP) of the micropipe region with the *c*-axis of the 4H-SiC marked. Inset is of the same region showing an optical image of the associated arrow defect with a 20 µm scale bar. b) The s-SNOM topography of the yellow boxed region in the UV-PL, and c) the s-SNOM topography of the red boxed region in the topography image in (b). d) The s-SNOM amplitude (top) and phase (bottom) of (b) at two frequencies, $\omega = 891$ cm^{-1} (left) and $\omega = 944$ cm^{-1} (right). All scale bars in (d) are 5 µm. e) The s-SNOM amplitude (top) and phase (bottom) of (c) at the same two frequencies, depicting the single micropipe in (c). Note: there is a slight lateral shift of 0.4 µm between the data collected at $\omega = 891$ cm^{-1} and $\omega = 944$ cm^{-1} . The micropipe (µP), the rims most likely due to a surface morphological effect (M), threading edge (TE), and threading screw (TS) dislocations are all marked. All scale bars in (e) are 1 µm. The s-SNOM amplitude and phase scale refer to all images in (d) and (e).

was collected for the yellow-boxed region containing the micropipes (Figure 6b), revealing that they (largest dark spots in topography) have a range of precise sizes and multiple smaller defects associated with them that were unresolvable in the UV-PL images.

The optical near-field images in Figure 6b,d were taken at frequencies of ω = 891 cm^{-1} (left) and ω = 944 cm^{-1} (right). Noticeably, at 944 cm^{-1} a new feature appears that was not initially observed around the carrot defect: that of wave-like structures centered at the largest micropipe that becomes distorted along the axis of the projected illumination onto the sample surface (marked by the red arrow in the corner of the phase image). These waves are not observed in topography and are most likely propagating SPhPs launched due to reflection of the tip-scattered incident light by the micropipe. This results in an interference with the illuminating $\omega = 944$ cm^{-1} wave, coinciding with the observed interference pattern.[56] In the direction of illumination, the fringe spacing of the waves is ≈2.8 µm, indicating it could either be an edge or tip launched SPhP in SiC, as it is between the frequencies for the two modes.[54,56,57] From our calculations of the SPhP frequency,[54] given the unmodified dielectric function of 4H-SiC from Tiwald et al.,[53] at $\omega = 944$ cm^{-1} the spacing of an edge launched SPhP would be 3.8 µm, while a tip launched mode would be ≈1.9 µm. However, at the lower energy, $\omega = 891$ cm^{-1} frequency, the spacing of edge launched SPhP fringes would be ≈10.1 µm, and thus, no noticeable fringes would be anticipated within our s-SNOM images. At such small wavevectors (long SPhP wavelengths) the sharp tip cannot efficiently couple to SPhPs, consistent with our observations. Additionally, now that SPhPs have been clearly identified around the micropipes, it becomes apparent that other defects also show similar, albeit less noticeable, wave-like structures. For instance, near the SR of the carrot defect a frequency dependent SPhP response is observable, where at 891 cm^{-1} no fringes are visible (Figure 4a), yet at 944 cm^{-1} thick parallel fringes of alternating dark and bright regions can be seen below the prismatic fault in both the amplitude and phase images (Figure 4b). These fringes are spaced ≈2 µm apart, consistent with tip-launched SPhPs. The spacing of the observed SPhP modes suggests that while the micropipe defects could interact with both tip and edge launched SPhPs, the prismatic fault of the carrot defect primarily interacts with tip launched SPhPs. Altogether, this near-field data provides strong evidence that extended defects will interfere with phonon-based SiC optical applications[27b,58] such as SPhP resonators,[22a,32a,c] or superlenses,[59] as the micropipes would act as local SPhP sources or scattering centers.

Additional features are observed near the micropipe defects at both s-SNOM frequencies, such as small dark spots. A magnified near-field image of a single micropipe is provided to analyze these features in more detail (Figure 6c,e). While these features are observed in the topography as well as the near-field amplitude and phase, there is a spectral difference between the dark spots (see Section S3, Supporting Information, for additional detail). All the spots have a strong near-field amplitude contrast at 891 cm^{-1}, while only some have a strong amplitude contrast at 944 cm^{-1}. Additionally, in phase, the spots differentiate into two distinct types, where the larger spots that are nonuniform in shape have a much weaker near-field signal than the smaller uniform spots. In topography, there is no distinguishing between the two types of spots, other than their size. When the sizes of the observed spot defects are measured at 891 cm^{-1}, two size ranges become apparent, and those ranges bin perfectly into weak phase response and strong phase response. The first are a set of large, 11 000 nm^2 defects with a density of 2800 cm^{-2} with a smaller near-field phase response, and the second are small 1300 nm^2 defects with a density of 25 000 cm^{-2} with a larger near-field phase response. Additionally, the spots with a larger near-field response at 891 cm^{-1} have a greater spectral difference, as they are the spots that are more difficult to observe in amplitude at 944 cm^{-1}. While it has been previously shown that topography can identify TSDs, it typically requires confirmation using KOH etching.[49] Here, the difference in spectral signature in the observed spots suggests that TSDs can be differentiated from nondefect topographic features given the differences in spectral signature between spot types. The data suggests that the smaller spot features with a larger phase response and an observed spectral shift could be assigned to TSDs, identifying s-SNOM as a more complete nondestructive method for determining the locations of TSDs than topography alone.[48a,49]

3. Conclusions

Here we have demonstrated that scattering-type s-SNOM is an emerging characterization technique that allows for simultaneous topographic and spectroscopic investigations of solid-state materials with nanoscale resolution. Using s-SNOM, we characterized extended defects in an unintentionally doped epitaxial layer of 4H-SiC, similar to those used in many power electronic devices. Without the need for additional characterization techniques, the s-SNOM technique found strong evidence for identifying step-bunching, variations in polytype near a stair-rod dislocation indicating the presence of recombination-induced stacking faults, the presence of threading screw dislocations and the potential to delineate TSDs from random topographic features. We also observed surface phonon polariton propagation due to incident infrared light interacting with defects such as micropipes or the prismatic fault associated with a carrot defect. The spectroscopic information was obtained by collecting spatial maps over a range of incident frequencies within the Reststrahlen band of the material, and the collected signal was limited not by the diffraction limit, such as would be the case with UV-PL, but instead only by the radius of curvature of the AFM tip employed, which is typically on the order of 20 nm. In the s-SNOM technique, the imaging of defects due to changes in contrast of the near-field amplitude and phase is most sensitive within the Reststrahlen band of the material. However, there is a frequency dependent response to the defects that are observed around the carrot, micropipe, and surrounding extending defects in the 4H-SiC. The observed threading screw dislocations are most differentiable at longer wavelengths, where the images are less masked by SPhPs or influenced by polytype changes. Contrariwise, polytype and/or free carrier changes, such as those induced within an RISF, are more clearly observed at frequencies closer to the LO phonon, where the small permittivity values lend themselves to the modifications that occur due to stacking order changes and free carrier induced Drude effects. Additionally, fringes from propagating SPhPs are also observed more easily at frequencies closer to the LO phonon due to the fact that the shorter SPhP wavelengths have larger wavevectors and couple more efficiently with the sharp AFM tip. Thus, s-SNOM allows us to investigate defects present in 4H-SiC presented here, but it is also possible to do the same with other semiconductor materials and devices, adding s-SNOM as a defect characterization tool that can simultaneously provide for high spatial resolution microscopy and spectroscopy.

Overall, the interaction of extended defects with infrared light detected via the s-SNOM technique implies that the performance of optical devices at phonon frequencies will be strongly dependent upon light-matter interactions occurring near extended defects. For future work studying the spectral dependence of extended defects at IR frequencies, a broadband IR laser can be implemented in conjunction with the s-SNOM tool and an interferometer, acting as an FTIR spectrometer. This technique is referred to as nano-FTIR,[19b,60] and offers the ability to collect a broadband spectrum from each given spatial location, but again with the same ≈20 nm spatial resolution. Both s-SNOM and nano-FTIR would be beneficial additions to current investigations of semiconductor materials for high temperature and high power applications, such as SiC and emerging materials.[2a,3a,b] Specifically, an investigation of additional wide bandgap semiconductors, such as GaN[38] or different Ga_2O_3 polytypes[61] would be possible with current techniques, as at least a portion of the Reststrahlen bands for each is above 560 cm^{-1}, which is the low-frequency cutoff for current compact, broadband IR lasers employed in nano-FTIR (Figure S2, Supporting Information).[35a-c,38,55,62] Such studies would be valuable as the scientific community seeks to advance these materials for future power applications as well as for emerging single-photon emission in quantum optics applications and mid- and far-IR optical and nanophotonic concepts.

4. Experimental Section

UV-PL: The UV-PL maps were collected by illuminating the 1.2 mm^2 field of view with a 330 nm, 500 mW output of a Coherent Saber argon-ion laser, directed at the sample at ≈30° off normal. The PL was collected through a 50×, 0.5 NA Mitutoyo objective and passed through either a 590 nm long-pass or 445 nm band-pass filter (40 nm bandwidth) before being collected by a liquid-N_2 cooled charge-coupled detector (CCD) imaging array.

TEM: A cross-sectional TEM sample was acquired using an FEI Nova 600 Dual-beam FIB from the stair-rod end of the extended carrot defect, with the offcut direction (11–20) perpendicular to the prepared TEM sample plain. The TEM imaging was acquired with a JEOL 2200F TEM at 200 keV and a Nion UltraSTEM at 100 keV. The sample was damaged (amorphized) after imaging.

s-SNOM: To obtain infrared images with a subwavelength spatial resolution on the nanometer scale, a commercial scattering-type scanning near-field optical microscope (Neaspec) was applied. The setup was based on an atomic force microscope, working in the intermittent contact regime with a metallized Si tip (Arrow NCPt, NanoAndMore), oscillating at frequency ω near its resonance frequency. The oscillation amplitude was set to about 40 nm. Infrared light at various wavelengths was generated by tunable quantum cascade laser sources (Daylight solutions, laser power adjusted to $P \approx 4$–5 mW) and focused down to the tip using a parabolic mirror. A HgCdTe detector (Infrared Associates) was employed to detect the light backscattered from the tip. To obtain background-free infrared near-field amplitude and phase images, an interferometric pseudoheterodyne setup[20] was employed and the signal from the back-scattered light was demodulated at higher harmonics n of the tip oscillation frequency $n\omega$, while scanning the tip relative to the sample.

ECCI: Structural properties of the structures films along with dislocation densities of each polarity were investigated with electron channeling contrast imaging. In this technique, a conventional scanning electron microscope (FEI Nova 600 NanoLab SEM) and electron backscatter diffraction (EBSD) detector (hkl Technology Nordlys) were used to detect changes in diffracted electron yield due to lattice strain induced by defects. The sample was tilted to a small deviation from its Bragg angle, in this case 70° (it was SEM configuration dependent). All ECCI and SE measurements were made after the s-SNOM measurements.

Calculations: To model the bulk near-field amplitude $s_n(\varepsilon)/s_n^{\mathrm{Si}}$ and phase spectra $\phi_n(\varepsilon) - \phi_n^{\mathrm{Si}}$ ($n = 3$) for SiC-3C and 4H, the finite dipole model[52] was used. The dielectric data for SiC-3C and 4H were derived by fitting the FTIR spectra of a free-standing SiC-4H epilayer and a 3.5 µm thick SiC-3C film on a Si substrate.

Supporting Information

Supporting Information is available from the Wiley Online Library or from the author.

Acknowledgements

B.H. and C.E.M. contributed equally to this work. J.D.C., A.J.G., R.E.S., J.K.H., and N.M. acknowledge support from the Office of Naval Research, which was administered by the U.S. Naval Research Laboratory Base Program and Nanoscience Institute. J.D.C. gratefully acknowledges support from the NRL Long-Term Training (Sabbatical Program), which allowed him to perform this work. B.H., M.L., and T.T. gratefully acknowledge financial support from the DFG (German Science Foundation) within the collaborative research center SFB 917 "Nanoswitches." Furthermore, T.T. thanks the Ministry of Innovation, Science, Research and Technology of the German State of North Rhine-Westphalia for financial support.

Conflict of Interest

The authors declare no conflict of interest.

Keywords

extended defects, scanning near-field optical microscopy, silicon carbide, surface phonon polaritons, ultraviolet photoluminescence

Received: September 5, 2019
Revised: November 27, 2019
Published online: January 20, 2020

---

[1] a) K. Shenai, M. Dudley, R. F. Davis, *ECS J. Solid State Sci. Technol.* **2013**, *2*, N3055; b) J. Hudgins, R. De Doncker, *IEEE Ind. Appl. Mag.* **2012**, *18*, 18.

[2] a) T. Kimoto, *Jpn. J. Appl. Phys.* **2015**, *54*, 040103; b) X. She, A. Q. Huang, Ó. Lucía, B. Ozpineci, *IEEE Trans. Ind. Electron.* **2017**, *64*, 8193.

[3] a) M. Meneghini, G. Meneghesso, E. Zanoni, *Power GaN Devices*, Springer International Publishing, Cham, Switzerland **2017**; b) M. Higashiwaki, A. Kuramata, H. Murakami, Y. Kumagai, *J. Phys. D: Appl. Phys.* **2017**, *50*, 333002; c) H. Von Wenckstern, *Adv. Electron. Mater.* **2017**, *3*, 1600350; d) S. Pearton, J. Yang, P. H. CaryIV, F. Ren, J. Kim, M. J. Tadjer, M. A. Mastro, *Appl. Phys. Rev.* **2018**, *5*, 011301; e) T. J. Flack, B. N. Pushpakaran, S. B. Bayne, *J. Electron. Mater.* **2016**, *45*, 2673.

[4] a) F. Bechstedt, P. Käckell, A. Zywietz, K. Karch, B. Adolph, K. Tenelsen, J. Furthmüller, *Phys. Status Solidi B* **1997**, *202*, 35; b) O. J. Glembocki, M. Skowronski, S. Prokes, D. K. Gaskill, J. D. Caldwell, *Mater. Sci. Forum* **2006**, *527-529*, 347.

[5] R. Stahlbush, N. Mahadik, presented at *2018 IEEE Int. Reliability Phys. Symp. (IRPS)*, Burlingame, CA, March **2018**.

[6] a) G. Wagner, M. Baldini, D. Gogova, M. Schmidbauer, R. Schewski, M. Albrecht, Z. Galazka, D. Klimm, R. Fornari, *Phys. Status Solidi A* **2014**, *211*, 27; b) S. Usami, Y. Ando, A. Tanaka, K. Nagamatsu, M. Deki, M. Kushimoto, S. Nitta, Y. Honda, H. Amano, Y. Sugawara, *Appl. Phys. Lett.* **2018**, *112*, 182106.

[7] a) J. D. Caldwell, L. Lindsay, V. Giannini, I. Vurgaftman, T. L. Reinecke, S. A. Maier, O. J. Glembocki, *Nanophotonics* **2015**, *4*, 44; b) R. Hillenbrand, *Ultramicroscopy* **2004**, *100*, 421.

[8] A. Lohrmann, B. Johnson, J. McCallum, S. Castelletto, *Rep. Prog. Phys.* **2017**, *80*, 034502.

[9] a) S. Ferrero, S. Porro, F. Giorgis, C. Pirri, P. Mandracci, C. Ricciardi, L. Scaltrito, C. Sgorlon, G. Richieri, L. Merlin, *J. Phys.: Condens. Matter* **2002**, *14*, 13397; b) J. D. Caldwell, R. Stahlbush, N. Mahadik, *J. Electrochem. Soc.* **2012**, *159*, R46.

[10] a) K. X. Liu, R. E. Stahlbush, M. E. Twigg, J. D. Caldwell, E. R. Glaser, K. D. Hobart, F. J. Kub, *J. Electron. Mater.* **2007**, *36*, 297; b) A. Iijima, I. Kamata, H. Tsuchida, J. Suda, T. Kimoto, *Philos. Mag.* **2017**, *97*, 2736.

[11] a) T. Ryan, J. Hennessy, C. Harrison, S. Y. Wang, G. Webster, A. Majima, *Mater. Sci. Forum* **2007**, *556-557*, 229; b) M. Tajima, E. Higashi, T. Hayashi, H. Kinoshita, H. Shiomi, *Mater. Sci. Forum* **2006**, *527-529*, 711; c) R. E. Stahlbush, K. X. Liu, Q. Zhang, J. J. Sumakeris, *Mater. Sci. Forum* **2007**, *556-557*, 295.

[12] a) K. X. Liu, R. E. Stahlbush, S. I. Maximenko, J. D. Caldwell, *Appl. Phys. Lett.* **2007**, *90*, 153503; b) K. X. Liu, R. E. Stahlbush, K.-K. Lew, R. L. Myers-Ward, B. L. VanMil, K. D. Gaskill, C. R. Eddy, *J. Electron. Mater.* **2008**, *37*, 730.

[13] S. I. Maximenko, J. A. Freitas Jr., P. B. Klein, A. Shrivastava, T. S. Sudarshan, *Appl. Phys. Lett.* **2009**, *94*, 092101.

[14] a) S. Ha, P. Mieszkowski, M. Skowronski, L. Rowland, *J. Cryst. Growth* **2002**, *244*, 257; b) M. Benamara, X. Zhang, M. Skowronski, P. Ruterana, G. Nouet, J. Sumakeris, M. Paisley, M. O'Loughlin, *Appl. Phys. Lett.* **2005**, *86*, 021905.

[15] a) B. Simkin, M. Crimp, *Ultramicroscopy* **1999**, *77*, 65; b) R. Glass, L. Kjellberg, V. Tsvetkov, J. Sundgren, E. Janzén, *J. Cryst. Growth* **1993**, *132*, 504.

[16] G. Naresh-Kumar, D. Thomson, M. Nouf-Allehiani, J. Bruckbauer, P. Edwards, B. Hourahine, R. Martin, C. Trager-Cowan, *Mater. Sci. Semicond. Process.* **2016**, *47*, 44.

[17] a) A. J. Wilkinson, P. B. Hirsch, *Micron* **1997**, *28*, 279; b) Y. Picard, M. Twigg, J. Caldwell, C. Eddy Jr., P. Neudeck, A. Trunek, J. Powell, *Appl. Phys. Lett.* **2007**, *90*, 234101; c) J. Hite, M. Mastro, C. Eddy Jr., *J. Cryst. Growth* **2010**, *312*, 3143.

[18] a) C. Trager-Cowan, F. Sweeney, P. Trimby, A. Day, A. Gholinia, N.-H. Schmidt, P. Parbrook, A. Wilkinson, I. Watson, *Phys. Rev. B* **2007**, *75*, 085301; b) Y. Picard, J. D. Caldwell, M. Twigg, C. Eddy Jr., M. Mastro, R. Henry, R. Holm, P. Neudeck, A. Trunek, J. Powell, *Appl. Phys. Lett.* **2007**, *91*, 094106.

[19] a) F. Keilmann, R. Hillenbrand, *Philos. Trans. R. Soc. A* **2004**, *362*, 787; b) F. Huth, A. Govyadinov, S. Amarie, W. Nuansing, F. Keilmann, R. Hillenbrand, *Nano Lett.* **2012**, *12*, 3973; c) J. Wessel, *J. Opt. Soc. Am. B* **1985**, *2*, 1538.

[20] N. Ocelic, A. Huber, R. Hillenbrand, *Appl. Phys. Lett.* **2006**, *89*, 101124.

[21] T. Folland, L. Nordin, D. Wasserman, J. D. Caldwell, *J. Appl. Phys.* **2019**, *125*, 191102.

[22] a) J. D. Caldwell, O. J. Glembocki, Y. Francescato, N. Sharac, V. Giannini, F. J. Bezares, J. P. Long, J. C. Owrutsky, I. Vurgaftman, J. G. Tischler, *Nano Lett.* **2013**, *13*, 3690; b) R. Hillenbrand, T. Taubner, F. Keilmann, *Nature* **2002**, *418*, 159.

[23] S. A. Maier, *Plasmonics: Fundamentals and Applications*, Springer Science & Business Media, New York, NY, USA **2007**.

[24] a) J. Chen, M. Badioli, P. Alonso-González, S. Thongrattanasiri, F. Huth, J. Osmond, M. Spasenović, A. Centeno, A. Pesquera, P. Godignon, *Nature* **2012**, *487*, 77; b) Z. Fei, A. Rodin, G. Andreev, W. Bao, A. McLeod, M. Wagner, L. Zhang, Z. Zhao, M. Thiemens, G. Dominguez, *Nature* **2012**, *487*, 82; c) S. Dai, Z. Fei, Q. Ma, A. Rodin, M. Wagner, A. McLeod, M. Liu, W. Gannett, W. Regan, K. Watanabe, *Science* **2014**, *343*, 1125; d) A. J. Giles, S. Dai, I. Vurgaftman, T. Hoffman, S. Liu, L. Lindsay, C. T. Ellis, N. Assefa, I. Chatzakis, T. L. Reinecke, *Nat. Mater.* **2018**, *17*, 134.

[25] a) B. Hauer, T. Saltzmann, U. Simon, T. Taubner, *Nano Lett.* **2015**, *15*, 2787; b) J. Stiegler, A. Huber, S. L. Diedenhofen, J. Gomez Rivas, R. Algra, E. Bakkers, R. Hillenbrand, *Nano Lett.* **2010**, *10*, 1387.

[26] Y. Chen, Y. Francescato, J. D. Caldwell, V. Giannini, T. W. Maß, O. J. Glembocki, F. J. Bezares, T. Taubner, R. Kasica, M. Hong, *ACS Photonics* **2014**, *1*, 718.

[27] a) A. Huber, N. Ocelic, T. Taubner, R. Hillenbrand, *Nano Lett.* **2006**, *6*, 774; b) A. Huber, A. Ziegler, T. Köck, R. Hillenbrand, *Nat. Nanotechnol.* **2009**, *4*, 153; c) E. A. Muller, B. Pollard, H. A. Bechtel, P. van Blerkom, M. B. Raschke, *Sci. Adv.* **2016**, *2*, e1601006.

[28] F. Alfaro-Mozaz, P. Alonso-González, S. Vélez, I. Dolado, M. Autore, S. Mastel, F. Casanova, L. Hueso, P. Li, A. Y. Nikitin, *Nat. Commun.* **2017**, *8*, 15624.

[29] M. F. Finch, C. A. Saunders Filho, N. Premkumar, Y. Yang, B. A. Lail, presented at *2016 IEEE Int. Symp. Antennas and Propagation (APS/URSI)*, Fajardo, Puerto Rico, June **2016**.

[30] T. G. Folland, A. Fali, S. T. White, J. R. Matson, S. Liu, N. A. Aghamiri, J. H. Edgar, R. F. Haglund, Y. Abate, J. D. Caldwell, *Nat. Commun.* **2018**, *9*, 4371.

[31] a) S. Castelletto, B. C. Johnson, A. Boretti, *Adv. Opt. Mater.* **2013**, *1*, 609; b) M. Widmann, S.-Y. Lee, T. Rendler, N. T. Son, H. Fedder, S. Paik, L.-P. Yang, N. Zhao, S. Yang, I. Booker, *Nat. Mater.* **2015**, *14*, 164.

[32] a) T. Wang, P. Li, B. Hauer, D. N. Chigrin, T. Taubner, *Nano Lett.* **2013**, *13*, 5051; b) A. M. Dubrovkin, B. Qiang, H. N. Krishnamoorthy, N. I. Zheludev, Q. J. Wang, *Nat. Commun.* **2018**, *9*, 1762; c) H. Sumikura, T. Wang, P. Li, A.-K. U. Michel, A. Heßler, L. Jung, M. Lewin, M. Wuttig, D. N. Chigrin, T. Taubner, *Nano Lett.* **2019**, *19*, 2549.

[33] J. L. O'brien, A. Furusawa, J. Vučković, *Nat. Photonics* **2009**, *3*, 687.

[34] K. Takemoto, Y. Nambu, T. Miyazawa, Y. Sakuma, T. Yamamoto, S. Yorozu, Y. Arakawa, *Sci. Rep.* **2015**, *5*, 14383.

[35] a) J.-J. Greffet, R. Carminati, K. Joulain, J.-P. Mulet, S. Mainguy, Y. Chen, *Nature* **2002**, *416*, 61; b) T. Wang, P. Li, D. N. Chigrin, A. J. Giles, F. J. Bezares, O. J. Glembocki, J. D. Caldwell, T. Taubner, *ACS Photonics* **2017**, *4*, 1753; c) J. A. Schuller, T. Taubner, M. L. Brongersma, *Nat. Photonics* **2009**, *3*, 658; d) A. D. Dunkelberger, C. T. Ellis, D. C. Ratchford, A. J. Giles, M. Kim, C. S. Kim, B. T. Spann, I. Vurgaftman, J. G. Tischler, J. P. Long, *Nat. Photonics* **2018**, *12*, 50; e) B. T. Spann, R. Compton, D. Ratchford, J. P. Long, A. D. Dunkelberger, P. B. Klein, A. J. Giles, J. D. Caldwell, J. C. Owrutsky, *Phys. Rev. B* **2016**, *93*, 085205; f) P. Li, X. Yang, T. W. Maß, J. Hanss, M. Lewin, A.-K. U. Michel, M. Wuttig, T. Taubner, *Nat. Mater.* **2016**, *15*, 870.

[36] N. Ocelic, R. Hillenbrand, *Nat. Mater.* **2004**, *3*, 606.

[37] T. Dougakiuchi, Y. Kawada, G. Takebe, *Appl. Phys. Express* **2018**, *11*, 032001.

[38] S. Bensmann, F. Gaußmann, M. Lewin, J. Wüppen, S. Nyga, C. Janzen, B. Jungbluth, T. Taubner, *Opt. Express* **2014**, *22*, 22369.

[39] A. Fali, S. T. White, T. G. Folland, M. He, N. A. Aghamiri, S. Liu, J. H. Edgar, J. D. Caldwell, R. F. Haglund, Y. Abate, *Nano Lett.* **2019**, *19*, 7725.

[40] M. Lewin, B. Hauer, M. Bornhöfft, L. Jung, J. Benke, A.-K. Michel, J. Mayer, M. Wuttig, T. Taubner, *Appl. Phys. Lett.* **2015**, *107*, 151902.

[41] H. Tsuchida, I. Kamata, M. Nagano, *J. Cryst. Growth* **2007**, *306*, 254.

[42] P. G. Neudeck, J. A. Powell, *IEEE Electron Device Lett.* **1994**, *15*, 63.

[43] J. D. Caldwell, P. Klein, M. E. Twigg, R. E. Stahlbush, O. J. Glembocki, K. X. Liu, K. D. Hobart, F. Kub, *Appl. Phys. Lett.* **2006**, *89*, 103519.

[44] Y. Chen, N. Zhang, X. R. Huang, D. R. Black, M. Dudley, *Mater. Sci. Forum* **2009**, *600-603*, 301.

[45] a) M. Syväjärvi, R. Yakimova, E. Janzén, *J. Cryst. Growth* **2002**, *236*, 297; b) T. Kimoto, A. Itoh, H. Matsunami, *Appl. Phys. Lett.* **1995**, *66*, 3645.

[46] M. Twigg, Y. Picard, *J. Appl. Phys.* **2009**, *105*, 093520.

[47] J. Pernot, E. Bustarret, M. Rudziński, P. R. Hageman, P. K. Larsen, *J. Appl. Phys.* **2007**, *101*, 033536.

[48] a) R. Berechman, M. Skowronski, S. Soloviev, P. Sandvik, *J. Appl. Phys.* **2010**, *107*, 114504; b) I. Kamata, M. Nagano, H. Tsuchida, Y. Chen, M. Dudley, *J. Cryst. Growth* **2009**, *311*, 1416.

[49] T. Aigo, W. Ito, H. Tsuge, H. Yashiro, M. Katsuno, T. Fujimoto, T. Yano, *Mater. Sci. Forum* **2013**, *740-742*, 629.

[50] a) U. Lindefelt, H. Iwata, S. Öberg, P. R. Briddon, *Phys. Rev. B* **2003**, *67*, 155204; b) M. Miao, S. Limpijumnong, W. R. Lambrecht, *Appl. Phys. Lett.* **2001**, *79*, 4360.

[51] a) J. D. Caldwell, A. Giles, D. Lepage, D. Carrier, K. Moumanis, B. A. Hull, R. E. Stahlbush, R. L. Myers-Ward, J. J. Dubowski, M. Verhaegen, *Appl. Phys. Lett.* **2013**, *102*, 242109; b) J. D. Caldwell, O. J. Glembocki, R. E. Stahlbush, K. D. Hobart, *Appl. Phys. Lett.* **2007**, *91*, 243509; c) J. D. Caldwell, R. E. Stahlbush, K. D. Hobart, O. J. Glembocki, K. X. Liu, *Appl. Phys. Lett.* **2007**, *90*, 143519; d) J. D. Caldwell, R. E. Stahlbush, M. G. Ancona, O. J. Glembocki, K. D. Hobart, *J. Appl. Phys.* **2010**, *108*, 044503.

[52] A. Cvitkovic, N. Ocelic, R. Hillenbrand, *Opt. Express* **2007**, *15*, 8550.

[53] T. E. Tiwald, J. A. Woollam, S. Zollner, J. Christiansen, R. Gregory, T. Wetteroth, S. Wilson, A. R. Powell, *Phys. Rev. B* **1999**, *60*, 11464.

[54] A. Huber, B. Deutsch, L. Novotny, R. Hillenbrand, *Appl. Phys. Lett.* **2008**, *92*, 203104.

[55] M. Lewin, C. Baeumer, F. Gunkel, A. Schwedt, F. Gaussmann, J. Wueppen, P. Meuffels, B. Jungbluth, J. Mayer, R. Dittmann, *Adv. Funct. Mater.* **2018**, *28*, 1802834.

[56] A. Huber, N. Ocelic, D. Kazantsev, R. Hillenbrand, *Appl. Phys. Lett.* **2005**, *87*, 081103.

[57] V. E. Babicheva, S. Gamage, M. I. Stockman, Y. Abate, *Opt. Express* **2017**, *25*, 23935.

[58] T. Taubner, D. Korobkin, Y. Urzhumov, G. Shvets, R. Hillenbrand, *Science* **2006**, *313*, 1595.

[59] a) P. Li, M. Lewin, A. V. Kretinin, J. D. Caldwell, K. S. Novoselov, T. Taniguchi, K. Watanabe, F. Gaussmann, T. Taubner, *Nat. Commun.* **2015**, *6*, 7507; b) S. Dai, Q. Ma, Y. Yang, J. Rosenfeld, M. D. Goldflam, A. McLeod, Z. Sun, T. I. Andersen, Z. Fei, M. Liu, *Nano Lett.* **2017**, *17*, 5285.

[60] S. Amarie, F. Keilmann, *Phys. Rev. B* **2011**, *83*, 045404.

[61] T. Azuhata, K. Shimada, *Appl. Phys. Express* **2017**, *10*, 081101.

[62] J. Wueppen, B. Jungbluth, T. Taubner, P. Loosen, presented at *2011 Int. Conf. Infrared, Millimeter, and Terahertz Waves*, Houston, TX, October **2011**.